Supplementary Information for

Concurrent Selective Laser Sintering and Graphitization of Polyimide Microparticles into Functional and Flexible 3D Structures for Energy Storage and Sensing

Muxuan Yang,[a,b] Jinyu Bu,[b] Pushkar N. Dalal,[a] Leyi Deng,[a] Mingcheng Liu,[b] Laura Brady,[c] Weinan Xu[a,b,*]

[a] Department of Materials Science and Engineering, University of Tennessee, Knoxville, TN 37996, USA
[b] School of Polymer Science and Polymer Engineering, The University of Akron, OH 44325, USA
[c] Department of Chemical and Biomolecular Engineering, University of Tennessee, Knoxville, TN 37996, USA

Table S1. Hausner ratios of the PI microparticles and PI-$FeCl_3$ hybrid microparticles

Types of particles	Apparent density (g/cm^3)	Tapped density (g/cm^3)	Hausner ratio
PI	0.465	0.564	1.21
PI-$FeCl_3$	0.485	0.606	1.25

Table S2. Comparison of the Raman characteristics and sheet resistance of the 3D graphene in this work with representative literature reports on LIG.

Types of graphene	I_D/I_G ratio	Sheet resistance	Reference
3D graphene by SLS (this work)	0.54–0.83 (tunable)	21 Ω/sq	/
3D graphene-FeO_x by SLS (this work)	0.61–0.84	15.9 Ω/sq	/
LIG with flash Joule heating	0.33–0.84	150–600 Ω	S1
LIG from PI film	0.5–1.3	16–35 Ω/sq	S2
LIG from PI paper	0.6–0.8	145.8–18.5 Ω/sq	S3
3D LIG foam	0.6–1.0	(conductivity) 0.050 – 0.27 S/cm	S4

* Corresponding author email: wxu@utk.edu

Table S3. Comparison of the electrochemical performance of the supercapacitors based on our SLS fabrication method with related literature reports on LIG-based systems.

Materials	Areal capacitance (mF/cm^2)	Gravimetric capacitance (F/g)	Current density/ Scan rate	Electrolyte	Source
Fe-doped LIG	63.1	467	0.5 mA/cm^2	Gel	This Work
Fe-doped LIG	63.95	474	5mV/s	Gel	This Work
LEST graphene/PI	17.97	/	0.05 mA/cm^2	Gel	S5
LIG/MnO_2	85.88	/	0.4 mA/cm^2	Gel	S6
High porous LIG	22.2	/	0.05 mA/cm^2	Gel	S7
LIG	34	181	0.1 mA/cm^2	Aqueous	S8
N doped LIG	54.5	/	0.08 mA/cm^2	Gel	S9
B doped LIG	60.6	/	0.08 mA/cm^2	Gel	S9
Selective grown Mn_3O_4/LIG	65.79	/	0.4 mA/cm^2	Gel	S10
B/N co-doped LIG	87.2	/	0.5 mA/cm^2	Gel	S11

Table S4. Comparison of the stain sensor performance of our 3D TPU-graphene fabricated by SLS method with relevant literature reports

Materials	**Design**	**Gauge Factor**	**Detection Range (%)**	**Cyclic stability**	**Source**
3D TPU-graphene (90°)	Rectangle	3.6/26/95	27	>10000	This Work
3D TPU-graphene (0°)	Rectangle	15/128/680	23	>10000	This Work
Transferred LIG	Serpentine	128.9	20	3600	S12
Peeled off LIG/MPU	Rectangle	5-70	60	200	S13
Peeled off LIG/starch	Rectangle	134.2	0.6	1000	S14
Transferred LIG/Ecoflex	Fingerprint	4.51/43.9/191	50	>1500	S15
3D PEEK/LIG/PDMS	Rectangle	51/212.3	5	5000	S16
Transferred MoS_2/LIG/PDMS	Rectangle	236/1242	37.5	12000	S17

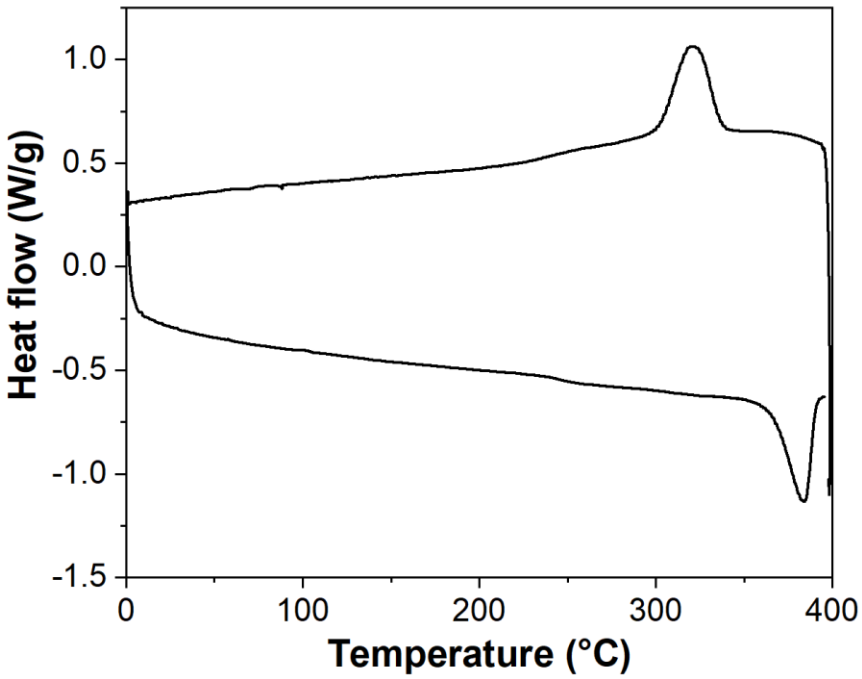

Figure S1. DSC characterization of the PI microparticles, which shows the T_g of PI is about 250 ºC, and the T_m is about 384 ºC. The crystallization peak during cooling cycle occurs at 320 ºC

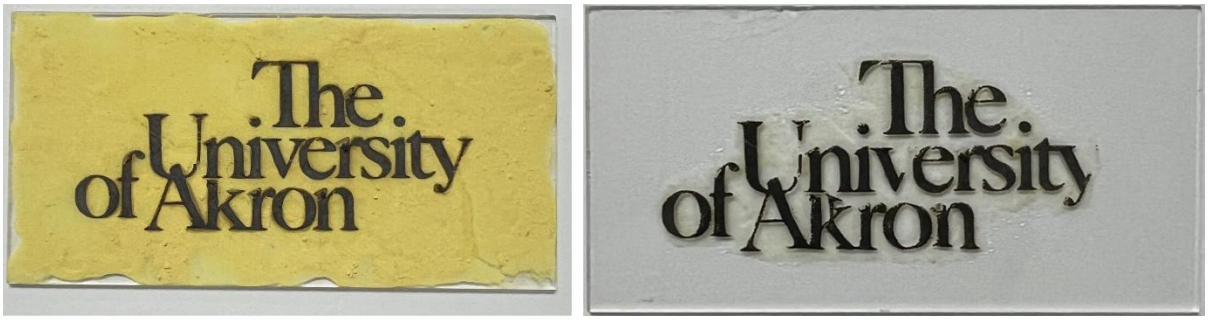

Figure S2. Photos of the SLS-fabricated graphene pattern on a glass substrate. The left image is before removing the excess PI microparticles in the background, and the right image is after removing the excess microparticles.

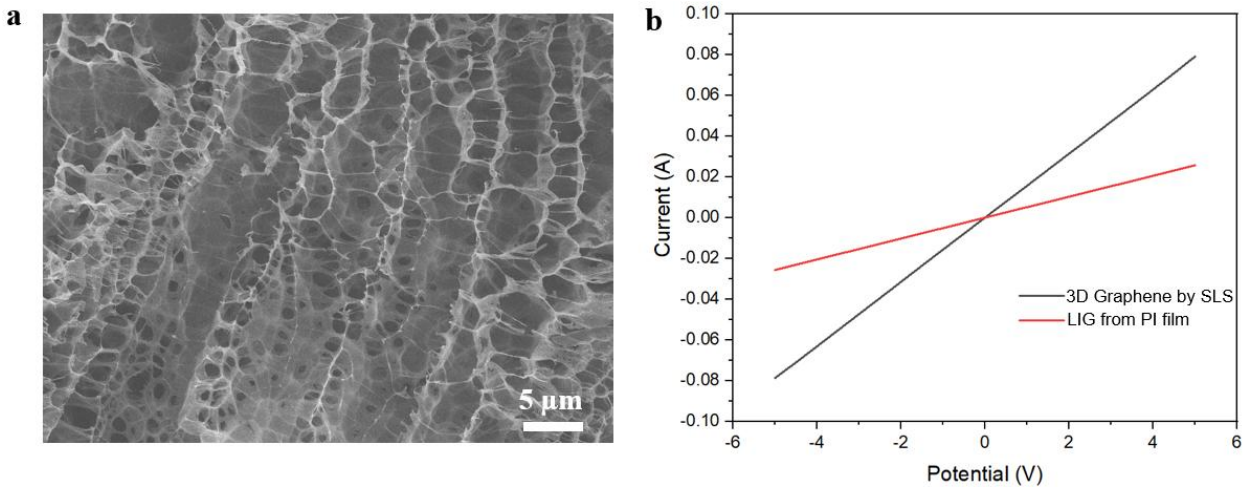

Figure S3. (a) SEM image of LIG film formed by laser scanning on a solid PI film using the same laser parameter as the SLS process. (b) Comparison of the I-V curves for the 3D graphene formed by SLS, and the LIG from PI film.

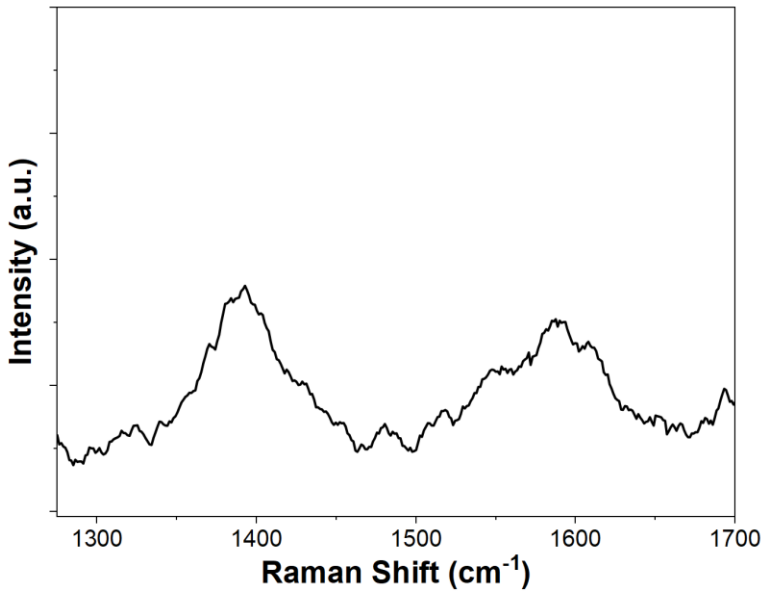

Figure S4. Raman spectrum of the LIG sample formed by using solid polyimide film as the precursor, with the same laser scanning parameters as our SLS process. The sample shows an I_D/I_G ratio of 1.17.

Analytical modeling of the laser-induced heat generation

In our system, we compared the laser-induced graphitization of conventional PI film, which is the commonly used method, with our unique method of using PI microparticles as the precursor. The results showed that our method is able to generate graphene with higher conductivity and different morphology compared with the conventional method.
To explain such differences, we conducted analytical modeling of the local heat generation of the two systems: the first one is a continuous PI film with a thickness of 125 μm; the second one is a monolayer of aggregated ~10 μm PI microparticles. For the case of PI microparticles, because of the poor heat spreading (total contact area between particles is small, leading to low effective in-plane and through-plane conductivity), as well as the smaller areal heat capacity, both of which lead to higher local temperature increase, which is explained in more detail below.

1. Laser irradiation on continuous PI film
The laser power $P = 2.3$ W, laser spot diameter is 250 μm, or the radius w = 125 μm. The total laser irradiation time per unit area is about 0.02 s. The thermal conductivity of polyimide k = 0.12 W/mK, its density ρ = 1420 kg/m^3, heat capacity c_p = 1090 J/kg K, so that the thermal diffusivity α = 7.8x10^{-8} m^2/s. The absorptance of polyimide to the laser is represented by A.
Diffusion length over 0.002 s:

$$\ell = \sqrt{\alpha t} \approx \sqrt{(7.8 \times 10^{-8})(0.002)} \approx 12.5\ \mu\text{m} < 125\ \mu\text{m}$$

So the semi-infinite 1D peak estimate is reasonable as an upper bound for the short-time surface peak.
1) Peak absorbed heat flux at the beam center
Gaussian peak irradiance:

$$I_0 = \frac{2P}{\pi w^2}$$

Peak absorbed heat flux:

$$q_0'' = AI_0 = A\frac{2P}{\pi w^2}$$

Numerically:

$$q_0'' \approx 9.37 \times 10^7 A\ \text{W/m}^2$$

2) Analytic surface temperature rise (semi-infinite, constant flux for time t)

$$\Delta T_s(t) = \frac{2q''}{k}\sqrt{\frac{\alpha t}{\pi}}$$

Compute the diffusion factor:

$$\sqrt{\frac{\alpha t}{\pi}} = \sqrt{\frac{(7.8 \times 10^{-8})(0.002)}{\pi}} \approx 7.05 \times 10^{-6}\ \text{m}$$

Then:

$$\Delta T_{\max}(0.002\ \text{s}) \approx \frac{2(9.37 \times 10^7 A)}{0.12}(7.05 \times 10^{-6}) \approx 1.1 \times 10^4 A\ \text{K}$$

If the absorptance of polyimide to the laser (455 nm) (A) is estimated to be 0.3, then

$$\Delta T_{\max} \approx 3300\ \text{K}$$

2. Laser irradiation on monolayer of PI particles

For the case of PI microparticles, because of the poor heat spreading (total contact area between particles is small, leading to low effective in-plane and through-plane conductivity), as well as the smaller areal heat capacity, both of which lead to higher local temperature increase, which is explained in more detail below.

1) Internal equilibration time of a 10 μm PI microparticles

Take PI thermal diffusivity $\alpha \approx 7.8 \times 10^{-8}$ m^2/s(same as before, using $k \approx 0.12$W/m·K, $\rho \approx 1420$kg/m^3, $c_p \approx 1090$J/kg·K).

For a particle diameter $d_p = 10\ \mu$m,

$$t_{\text{diff,p}} \sim \frac{d_p^2}{\alpha} = \frac{(1.0 \times 10^{-5})^2}{7.8 \times 10^{-8}} \approx 1.28 \times 10^{-3}\ \text{s}$$

So during a 0.002 s laser exposure, each particle is close to isothermal internally.

2) Replace "semi-infinite conduction" with a thin-layer energy balance

A monolayer behaves more like a thin absorbing layer with areal heat capacity, not a thick solid that can diffuse heat away during the pulse.

- $d_p = 10\ \mu$m is the monolayer thickness
- ϕ is the solid area/volume fraction of the monolayer (which is close to 0.6 for random close packing in 2D)
- PI volumetric heat capacity $\rho c_p \approx 1.55 \times 10^6$ J/m^{3}K

Then the effective areal heat capacity of the monolayer is:

$$C'' \approx (\rho c_p)\,(\phi d_p)$$

For example, with $\phi = 0.6$:

$$C'' \approx 1.55 \times 10^6 \times (0.6 \times 10 \times 10^{-6}) \approx 9.3\ \text{J/m}^2\text{K}$$

3) Laser heat input

With a Gaussian beam and 250 μm = 1/e² diameter, $w = 125\ \mu$m.

Peak irradiance:

$$I_0 = \frac{2P}{\pi w^2}$$

The peak absorbed flux (q_0'') needs to be modified with an effective absorptance A_{eff} for the *powder monolayer,* which can be quite different from a dense film due to voids/scattering.

$$q_0'' = A_{\text{eff}} I_0 = A_{\text{eff}} \frac{2P}{\pi w^2}$$

$$q_0'' \approx 9.37 \times 10^7\ A_{\text{eff}}\ \text{W/m}^2$$

4) Temperature rise over a short pulse (0.002 s)

For short times where convection/radiation is negligible, the monolayer center temperature rise is approximately:

$$\Delta T_{\max} \approx \frac{q_0''\, t}{C''}$$

Plugging in $t = 0.002$s and $C'' = (\rho c_p)(\phi d_p)$:

$$\Delta T_{\max} \approx \frac{(9.37 \times 10^7 A_{\text{eff}})(0.002)}{(1.55 \times 10^6)(\phi)(10 \times 10^{-6})}$$

This simplifies to:

$$\Delta T_{\max} \approx \frac{1.21 \times 10^4}{\phi}\ A_{\text{eff}}\ \text{K}$$

So with $\phi = 0.6$:

$$\Delta T_{\max} \approx 2.02 \times 10^4 \, A_{\text{eff}} \, \text{K}$$

Compared with the solid PI film case, where $\Delta T_{\max} \approx 3300$ K. Therefore, as long as the effective absorptance $A_{\text{eff}} > 0.163$, then the temperature increase of the PI particle monolayer would be higher than that of the solid PI film.

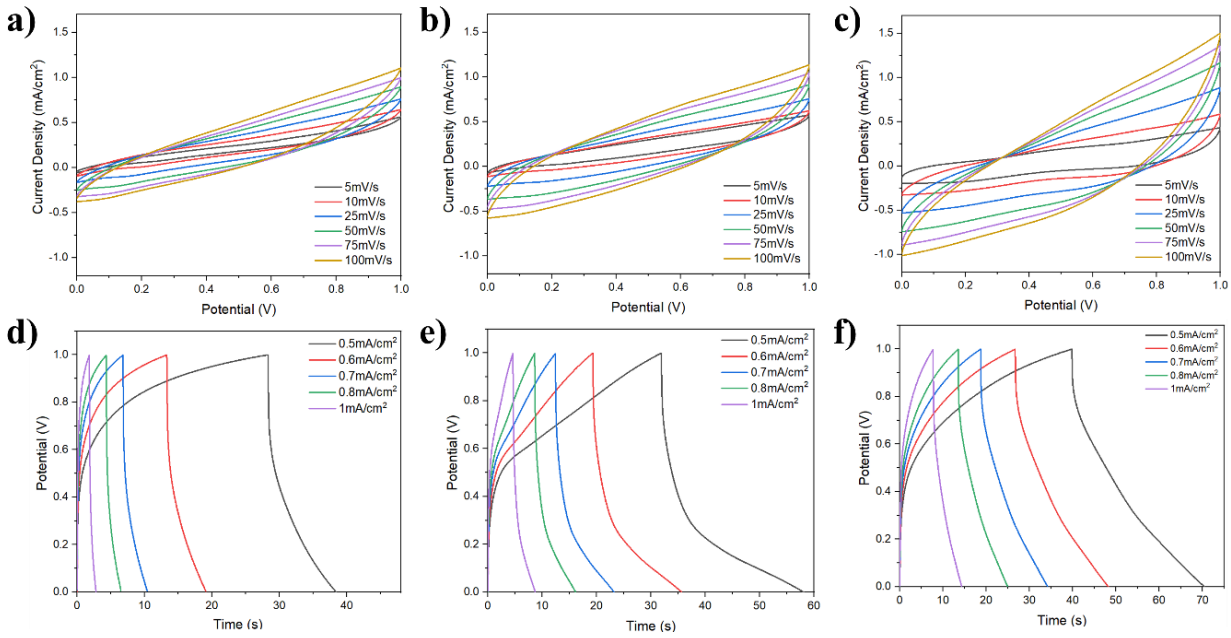

Figure S5. (a-c) CV curves at various scan rates from 5 mV/s to 100 mV/s of supercapacitors fabricated by (a) 1-layer SLS, (b) 2-layer SLS, and (c) 3-layer SLS. (d-f) GCV curves measured at different current densities of the supercapacitors fabricated by (d) 1-layer SLS, (e) 2-layer SLS, and (f) 3-layer SLS.

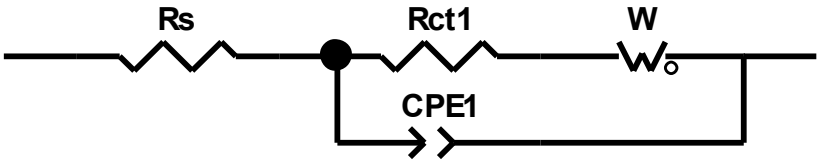

Figure S6. The equivalent circuit model used to fit the EIS curves of the supercapacitors show in Fig. 3h.

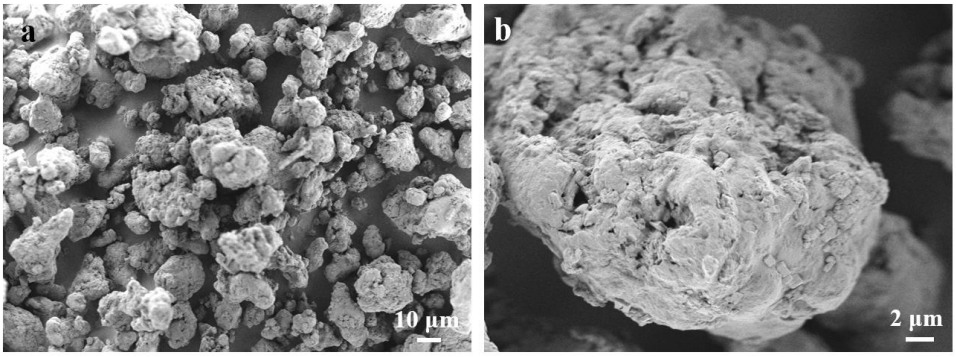

Figure S7. SEM image of the $FeCl_3$ modified PI microparticles at different magnifications.

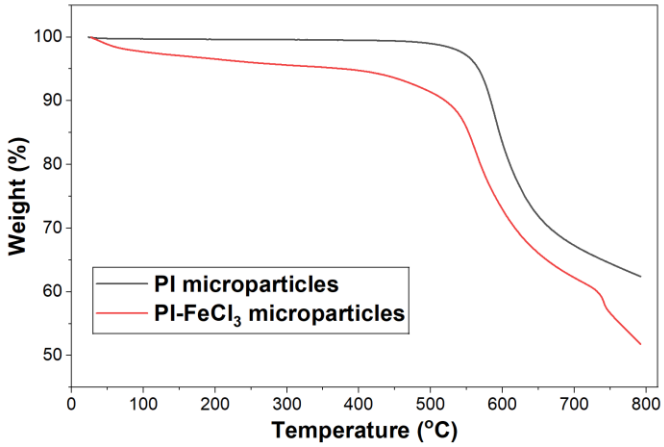

Figure S8. TGA curves of the PI microparticles with and without $FeCl_3$ modification.

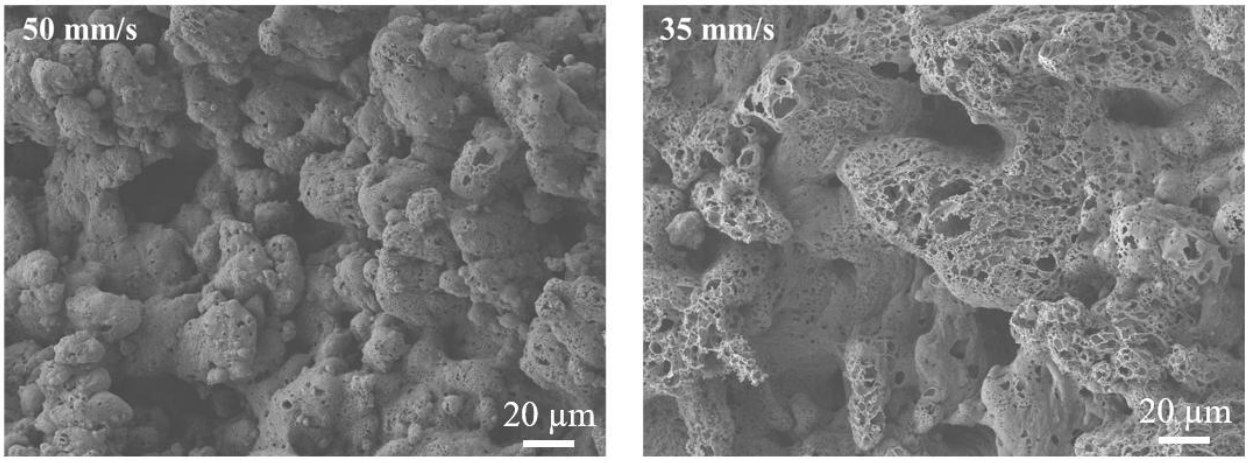

Figure S9. SEM images of Fe-doped 3D graphene fabricated at a laser speed of 50 mm/s (left) and 35 mm/s (right).

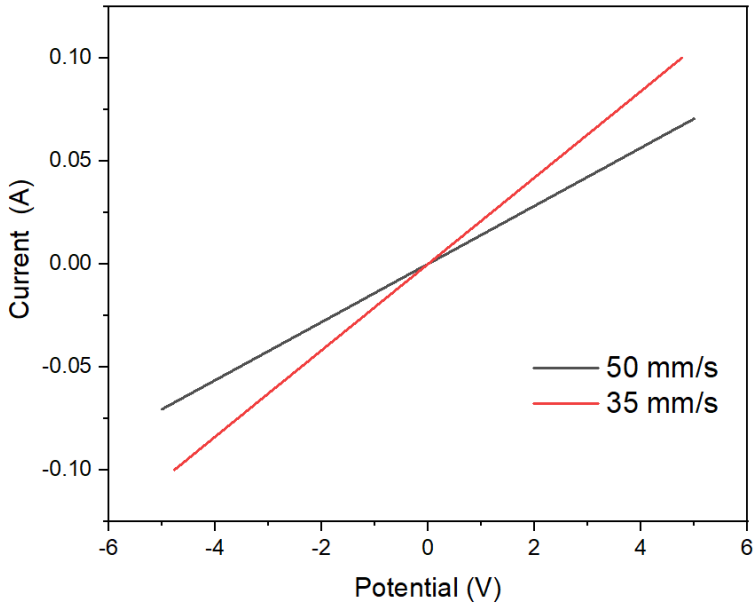

Figure S10. I-V curves of Fe-doped 3D graphene fabricated at a laser speed of 50 mm/s and 35 mm/s.

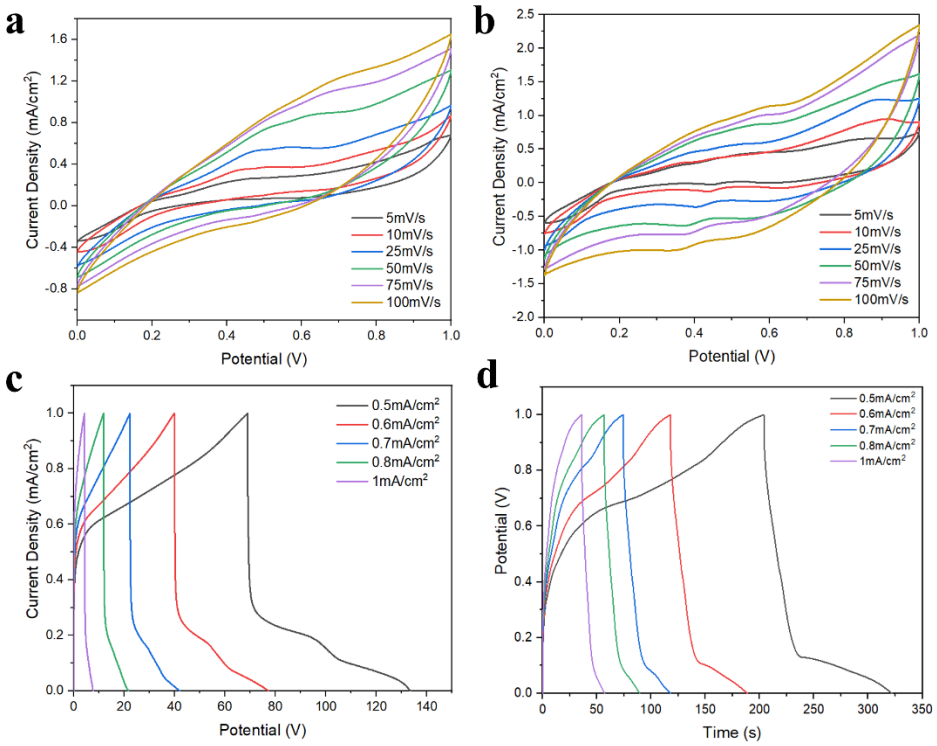

Figure S11. (a-b) CV curves at various scan rates of the flexible supercapacitors with Fe-doped 3D graphene electrodes fabricated at (a) 50 mm/s and (b) 35 mm/s. (d-e) GCV curves measured at different current densities of the supercapacitors with Fe-doped 3D graphene electrodes fabricated at (c) 50 mm/s and (d) 35 mm/s.

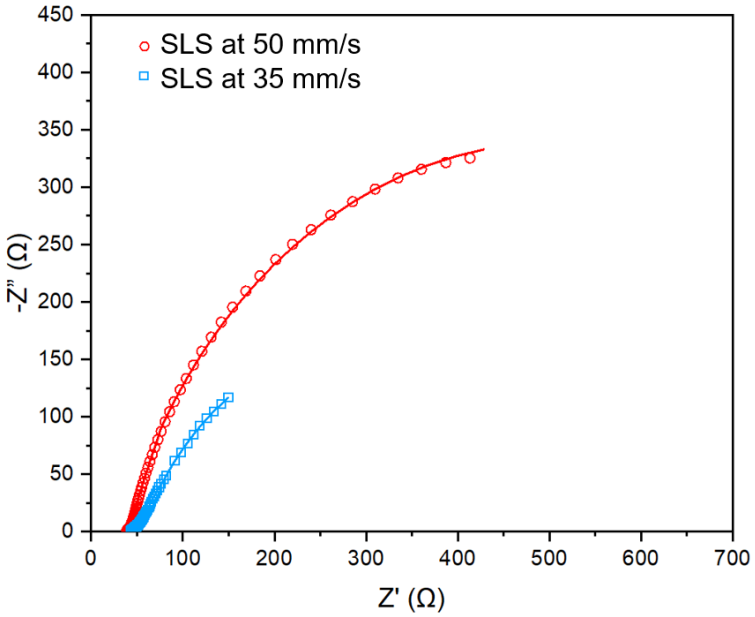

Figure S12. EIS curves of the supercapacitors fabricated by SLS with Fe-doped 3D graphene electrodes at two different laser scanning speeds.

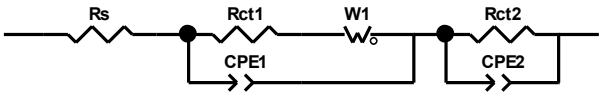

The equivalent circuit model used for fitting shown above, includes two charge transfer resistances: R_{ct1}, associated with surface-controlled energy storage, and R_{ct2}, linked to diffusion-controlled ion intercalation. Both devices showed low R_{ct1} values (16.21 Ω for 50 mm/s and 11.92 Ω for 35 mm/s), confirming that the porous structure promotes surface-dominated charge storage, in line with the CV results. However, R_{ct2} remained high for the 50 mm/s device (943.5 Ω), indicating limited ion intercalation, whereas the 35 mm/s device had a lower R_{ct2} (507.9 Ω), suggesting better ion accessibility.

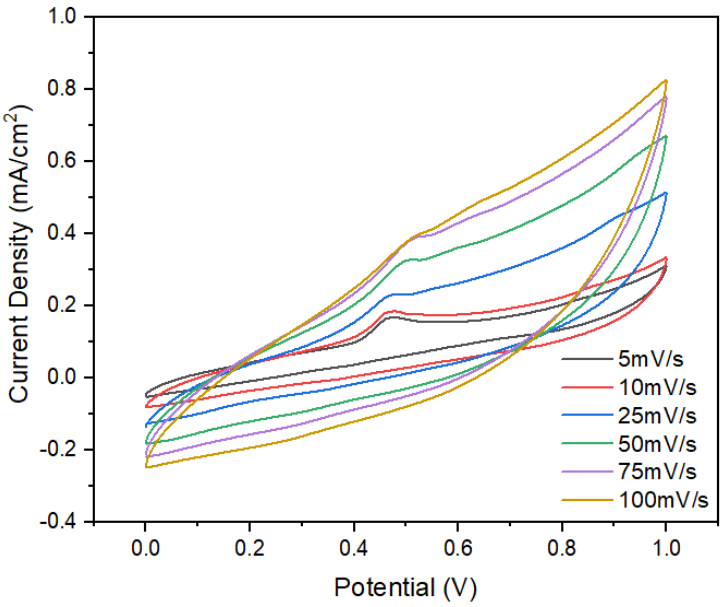

Figure S13. CV curves at various scan rates of the flexible supercapacitors with Co-doped 3D graphene electrodes. The precursors used for Co-doping is $Co(NO_3)_2$.

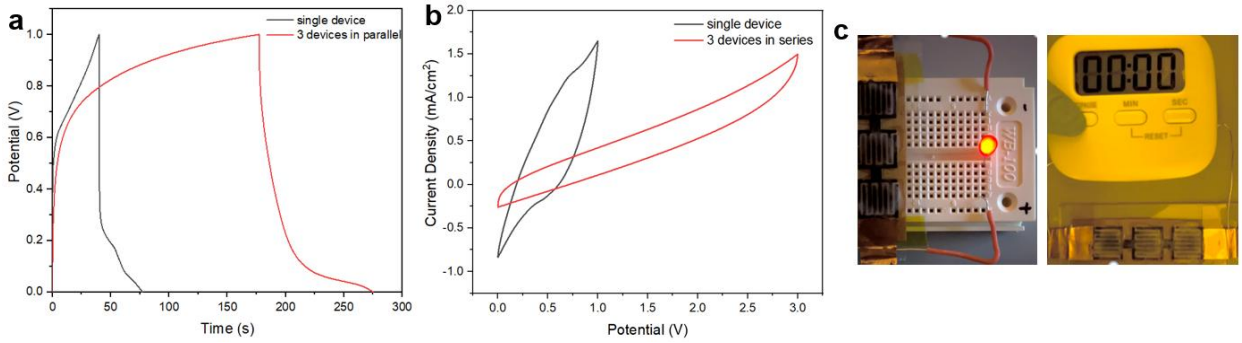

Figure S14. (a) Comparison of the GCD curves for supercapacitors with Fe-doped 3D graphene electrode in single form or 3-in-parallel form. (b) Comparison of the CV curves for supercapacitors with Fe-doped 3D graphene electrode in single form or 3-in-series form. (c) Demonstration of the powering for LED and laboratory timer with the 3-in-series supercapacitor.

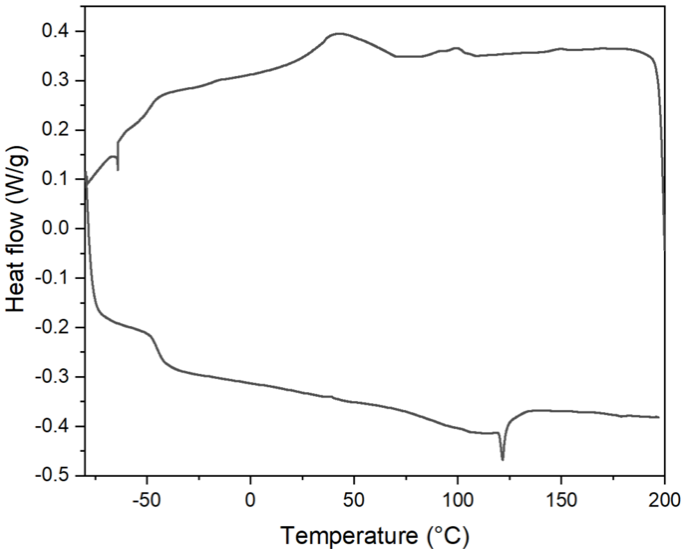

Figure S15. DSC curve of the TPU microparticles used in the sequential SLS 3D printing.

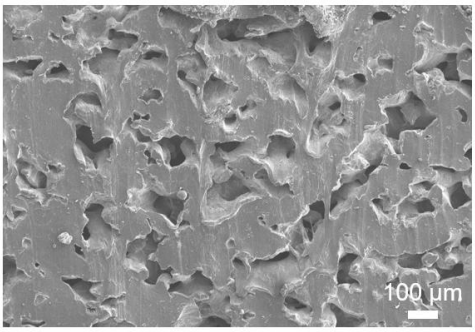

Figure S16. Cross-section SEM of the SLS-printed TPU part.

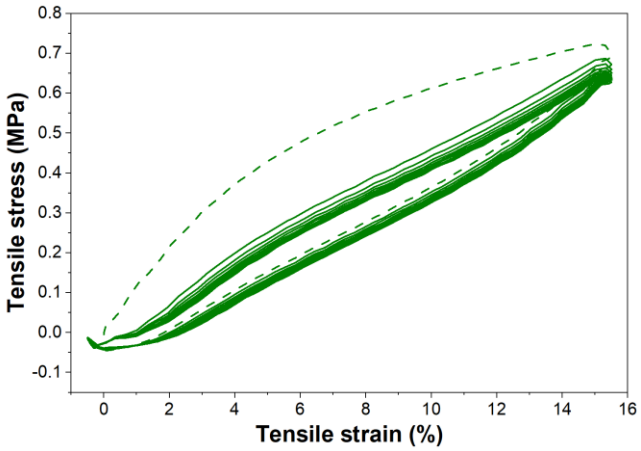

Figure S17. Cycling tests of SLS-printed TPU with a maximum strain of 15%, the first ten cycles of testing are shown.

References

1 L. Cheng, C. S. Yeung, L. Huang, G. Ye, J. Yan, W. Li, C. Yiu, F.-R. Chen, H. Shen, B. Z. Tang, Y. Ren, X. Yu and R. Ye, *Nat Commun*, 2024, **15**, 2925.

2 J. Lin, Z. Peng, Y. Liu, F. Ruiz-Zepeda, R. Ye, E. L. G. Samuel, M. J. Yacaman, B. I. Yakobson and J. M. Tour, *Nat Commun*, 2014, **5**, 5714.

3 Y. Wang, Y. Wang, P. Zhang, F. Liu and S. Luo, *Small*, 2018, **14**, 1802350.

4 D. X. Luong, A. K. Subramanian, G. A. L. Silva, J. Yoon, S. Cofer, K. Yang, P. S. Owuor, T. Wang, Z. Wang, J. Lou, P. M. Ajayan and J. M. Tour, *Advanced Materials*, 2018, **30**, 1707416.

5 N. Samartzis, M. Athanasiou, L. Sygellou and S. N. Yannopoulos, *ACS Appl. Nano Mater.*, 2024, **7**, 3782–3792.

6 Q. Liu, W. Wu, P. Luo, H. Yu, J. Wang, R. Chen and Y. Zhao, *Nanomaterials*, DOI:10.3390/nano15080584.

7 A. Velasco, Y. K. Ryu, A. Hamada, A. de Andrés, F. Calle and J. Martinez, *Nanomaterials*, DOI:10.3390/nano13050788.

8 J. R. J. UC, S. Bhat, Y. N. Sudhakar, A. Rao, V. Cyriac and S. De, *J Mater Sci*, 2025, **60**, 10944–10964.

9 M. Yuan, F. Luo, Z. Wang, H. Li, Y. Rao, J. Yu, Y. Wang, D. Xie, X. Chen and C.-P. Wong, *ACS Appl. Mater. Interfaces*, 2021, **13**, 22426–22437.

10 S. Remesh, N. N. Loganathan, V. Perumal, M. Ovinis, S. Karuppanan, T. N. J. I. Edison, P. B. Raja, M. N. M. Ibrahim, N. Arumugam and R. S. Kumar, *Journal of Energy Storage*, 2024, **77**, 109920.

11 M. Khandelwal, C. V. Tran, J. Lee and J. B. In, *Chemical Engineering Journal*, 2022, **428**, 131119.

12 T. Pinheiro, R. Correia, M. Morais, J. Coelho, E. Fortunato, M. G. F. Sales, A. C. Marques and R. Martins, *ACS Nano*, 2022, **16**, 20633–20646.

13 A. Dallinger, K. Keller, H. Fitzek and F. Greco, *ACS Appl. Mater. Interfaces*, 2020, **12**, 19855–19865.

14 H. Liu, H. Xiang, Z. Li, Q. Meng, P. Li, Y. Ma, H. Zhou and W. Huang, *ACS Sustainable Chem. Eng.*, 2020, **8**, 527–533.
15 W. Wang, L. Lu, Z. Li, L. Lin, Z. Liang, X. Lu and Y. Xie, *ACS Appl. Mater. Interfaces*, 2022, **14**, 1315–1325.
16 W. Yang, W. Zhao, Q. Li, H. Li, Y. Wang, Y. Li and G. Wang, *ACS Appl. Mater. Interfaces*, 2020, **12**, 3928–3935.
17 A. Chhetry, Md. Sharifuzzaman, H. Yoon, S. Sharma, X. Xuan and J. Y. Park, *ACS Appl. Mater. Interfaces*, 2019, **11**, 22531–22542.